A Study of Land Surface Albedo Conversion Formulas Using Three-Dimensional Canopy Radiative Transfer Modeling

Jennifer Adams, Nadine Gobron, and Corrado Mio

***Abstract*—Land surface albedo defines the fraction of short-wave radiation reflected by the Earth's surface and controls the surface energy balance; thus, it is important for environmental and climate scientific communities. Remote sensing is the only means to globally map land surface albedo, however for it to be of use to the aforementioned communities, it must be accurate with respect to Global Climate Observing System (GCOS) requirements. Sources of error are introduced in each step of the provision of land surface albedo products, whereby this letter intends to investigate sources of error introduced by the narrow-band-to-broad-band conversion formula step. The radiative transfer modeling of vegetation is used to simulate spectral albedo over complex 3-D vegetation canopies; then narrow-band-to-broad-band conversion formulas for numerous sensors are applied on the spectral albedo to compute the broad-band albedo (BBA), and the accuracy of formulas is investigated. Results indicate that the effectiveness of conversion formulas is determined by the sensor, depending on the placement and number of the sensor wavebands, the ecosystem complexity, and the broad-band range of the BBA.**

***Index Terms*—Modeling, Monte Carlo methods, remote sensing, vegetation.**

I. Introduction

LAND surface albedo is one of the Essential Climate Variables (ECVs) defined by the Global Climate Observing System (GCOS), in collaboration with the United Nations Framework Convention on Climate Change (UNFCC) and the Intergovernmental Panel of Climate Change (IPCC) [1]. It indicates the fraction of short-wave radiation reflected by the Earth's surface; thus, it is a forcing variable that controls the surface energy balance and is important for many environmental and climate scientific communities, for example, studies on climate sensitivity [2], drought [3], and fires [4]. Remote sensing is the only means to globally map land surface albedo, and since the first global albedo product produced from the NOAA/AVHRR instrument [5], many more sensors have provided or are providing global land surface products, including METEOSAT's MVIRI instrument [6]–[8], MSG's SEVIRI [9], CHRIS PROBA-V and SPOT VEGETATION [10], NASA's MODIS [11] and MISR [12], GlobAlbedo [13], and GLASS [14].

To be of use to environmental and climate research communities, broad-band albedo (BBA) is required in three broad-band spectrum ranges: visible (400–700 nm), near-infrared (NIR) (700–3000 nm), and short-wave (400–3000 nm). Albedo is further defined into directional–hemispherical reflectance (DHR) which describes albedo in conditions of solely direct illumination, isotropic bidirectional–hemispherical reflectance ($\mathrm{BHR_{iso}}$) which defines albedo in only diffuse illumination conditions, and bidirectional–hemispherical reflectance (BHR) which is a combination of the two [15]. The latter definition of albedo, BHR, is the quantity measured by ground instruments.

Under the GCOS initiative for high-quality accurate remotely sensed products, land surface albedo is required to be known at high absolute accuracy so that they are of use to scientific communities and the work of both UNFCC and IPCC [1]. Current GCOS accuracy criteria define that albedo must be accurate to within 5% (see [1, p. 71]). Albedo is not directly measured by remote sensing instruments; rather, it is inferred from a series of steps, including cloud masking, calibration, and atmospheric and anisotropic knowledge, whereby each step introduces a source of error. The final step is to use narrow-band-to-broad-band conversion formulas to convert spectral albedos to the aforementioned BBAs. Some studies have specifically investigated the error that this step may introduce [16], [17] by testing the formulas on a sample of spectra of many types of materials measured in the laboratory or from bidirectional-reflectance measurements. Results indicate that albedo can be computed using conversion formulas to within 2% [18] for most cases for these materials. However, so far, few tests have been applied to canopy albedo due to the lack of hyperspectral albedo data required for such a study.

Accordingly, this letter aims to investigate the effectiveness of narrow-band-to-broad-band conversion formulas for land surface albedo satellite retrievals in vegetation using radiative transfer (RT) modeling to simulate the albedo of vegetation canopies. A 3-D Monte Carlo ray tracing (MCRT) RT model is used to simulate DHR at fine spectral resolution for a variety of 3-D complex vegetation canopies; then conversion formulas are applied to the simulated spectral DHR in appropriate sensor

Manuscript received October 29, 2015; revised January 21, 2016; accepted January 27, 2016. Date of publication June 2, 2016; date of current version July 20, 2016.

J. Adams is with the Institute of Environment and Sustainability, Land Resource Management Unit, European Commission, Joint Research Centre (JRC), 21027 Ispra, Italy, and also with the Department of Geography, University College London, London WC1E 6BT, U.K. (e-mail: jennifer.adams@jrc.ec.europa.eu).

N. Gobron and C. Mio are with the Institute of Environment and Sustainability, Land Resource Management Unit, European Commission, Joint Research Centre (JRC), 21027 Ispra, Italy.

Color versions of one or more of the figures in this paper are available online at http://ieeexplore.ieee.org.

Digital Object Identifier 10.1109/LGRS.2016.2535160

TABLE I
VEGETATION CANOPY INFORMATION, DATA SOURCE, AND ILLUMINATION ANGLES (SAA: SOLAR AZIMUTH ANGLE, SZA: SOLAR ZENITH ANGLE)

Canopy	Season	Country	SZA (°)	SAA (°)
Birchstand	Summer	Estonia	36.6	270.7
Birchstand	Winter	Estonia	54.0	291.3
Pinestand	Summer	Estonia	36.6	299.1
Pinestand	Winter	Switzerland	47.0	151.9
Citrus	Summer	South Africa	50	0
Shrubland	Summer	Australia	36.6	283.9

wavebands and are compared to the albedo computed by integrating spectral DHR over each broad-band range.

II. MATERIALS AND METHODS

A 3-D canopy RT model is used to simulate DHR for a number of vegetation canopies. The RT model **raytran** [19] is an MCRT model that has been tested against *in situ* and goniometer measurements and has taken part in the RAdiation transfer Model Intercomparison (RAMI) exercise, which aims to assess the reliability of RT models [20], [21]. Three-dimensional vegetation MCRT models require the description of a vegetation canopy in terms of geometrical primitives [19]; therefore, "virtual" vegetation canopies were either generated or taken from the RAMI-IV phase for "actual canopies" [20], where descriptions of each canopy were taken from extensive field measurement campaigns, and then this information is converted to a form that RT models are able to digest, requiring the description of a canopy as a set of scatterers, each with their location, shape, size, and orientation, in addition to an interaction model which defines how the radiation is scattered, absorbed, or transmitted.

A birch-stand deciduous boreal forest located in Järvselja, Estonia, was inventoried in 2007 [22]–[24] during both summer and winter seasons, and a pine-stand coniferous forest in summer, also located in Järvselja, Estonia, was inventoried by Kuusk *et al.* [22]. Inventory data from a pine-stand coniferous forest in winter in Ofenpass, Switzerland, were collected by the authors of [25]–[27]. A citrus orchard canopy in South Africa was based on information collected by Stuckens *et al.* [28] in 2006/2007. A shrubland scene was generated, based on information taken from the Janina FLUXNET site in Australia [29]. Information on tree type, soil type, fractional coverage, and land surface type was extracted and used to generate the canopy. Canopies were selected to cover a range of seasonal and structural conditions, in addition to varying illumination angles. Table I lists the canopies identified, the source of information for each canopy, and illumination angles considered. Raytran was used to simulate DHR at 5 nm spectral resolution in the 400–2500 nm spectral range for each canopy under the specified illumination conditions.

Conversion formulas for a number of sensors were identified to be investigated for the purpose of this letter. Table II lists the sensor, the source of the conversion formulas, and the BBAs that each sensor provides, and Fig. 1 demonstrates the sensor response functions of each sensor. BBA can be defined as the albedo over a certain wavelength interval, weighted by the incoming solar irradiance. This integral can be approximated by

TABLE II
SENSORS, BROAD-BAND RANGE IN WHICH PRODUCTS ARE SUPPLIED, AND SOURCE OF CONVERSION FORMULAS. VIS REPRESENTS THE VISIBLE RANGE, (400–700 nm), NIR IS THE NEAR-INFRARED RANGE (700–2500 nm), AND SW IS THE SHORT-WAVE RANGE (400–2500 nm)

Sensor	Broadband range	Source	Temporal coverage
AATSR	vis,NIR,sw	[13]	2002-2012
AVHRR	vis,NIR,sw	[31]	1981-
PROBA-V	vis,NIR,sw	[10]	2002-
ETM+	vis,NIR,sw	[31]	1999-
GOES-8 Imager	vis,sw	[31]	1994-2004
MERIS	vis,NIR,sw	[13]	2002-2012
MVIRI 2-7	sw	[8]	1981-
SEVIRI 1-4	vis,NIR,sw	[32]	2004-
MISR	vis,NIR,sw	[31]	2000-
MODIS	vis,NIR,sw	[31]	2000-
VEGETATION	vis,NIR,sw	[10]	1998-2015

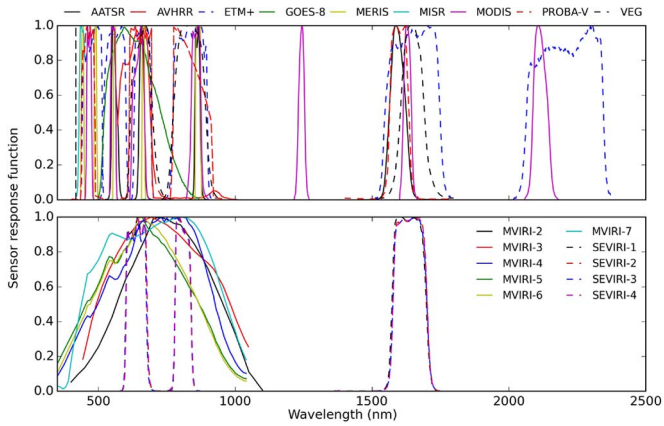

Fig. 1. Sensor response functions for all sensors.

the weighted sum of the integrand at discrete values of albedo [30]. Accordingly, BBA can be approximated from a linear combination of spectral albedo values in all available spectral bands. For DHR, BBA between two wavelengths λ_1 and λ_2 for specific illumination conditions (θ, φ) can be computed from the integral of discrete albedo values (α_{ref}) weighted by the incoming solar irradiance $(E^{\downarrow}(\lambda))$

$$\alpha_{\text{ref}[\lambda_1,\lambda_2]}(\theta,\varphi) = \frac{\int_{\lambda_1}^{\lambda_2} \alpha(\lambda,\theta,\varphi)E^{\downarrow}(\lambda)d\lambda}{\int_{\lambda_1}^{\lambda_2} E^{\downarrow}(\lambda)d\lambda}. \quad (1)$$

Accordingly, (1) was used to compute the "reference BBA" as the linear combination of simulated DHR albedo at 5 nm spectral resolution in the visible, NIR, and short-wave ranges. Spectral albedos were extracted in appropriate sensor wavebands, convolved with incoming solar irradiance; then, conversion formulas were applied for each broad-band spectral range, visible $(\text{BBA}_{\text{vis}})$, NIR $(\text{BBA}_{\text{nir}})$, and short-wave (BBA_{sw}), and compared against the "reference BBA." The relative normalized uncertainty (Δ) [%] was computed following (2), where α_{ref} determines the reference BBA and α_{mes} is the BBA computed from conversion formulas, and compliance with the 5% GCOS requirement was tested.

$$\Delta[\%] = \frac{\alpha_{\text{mes}} - \alpha_{\text{ref}}}{\alpha_{\text{ref}}} \cdot 100 \quad (2)$$

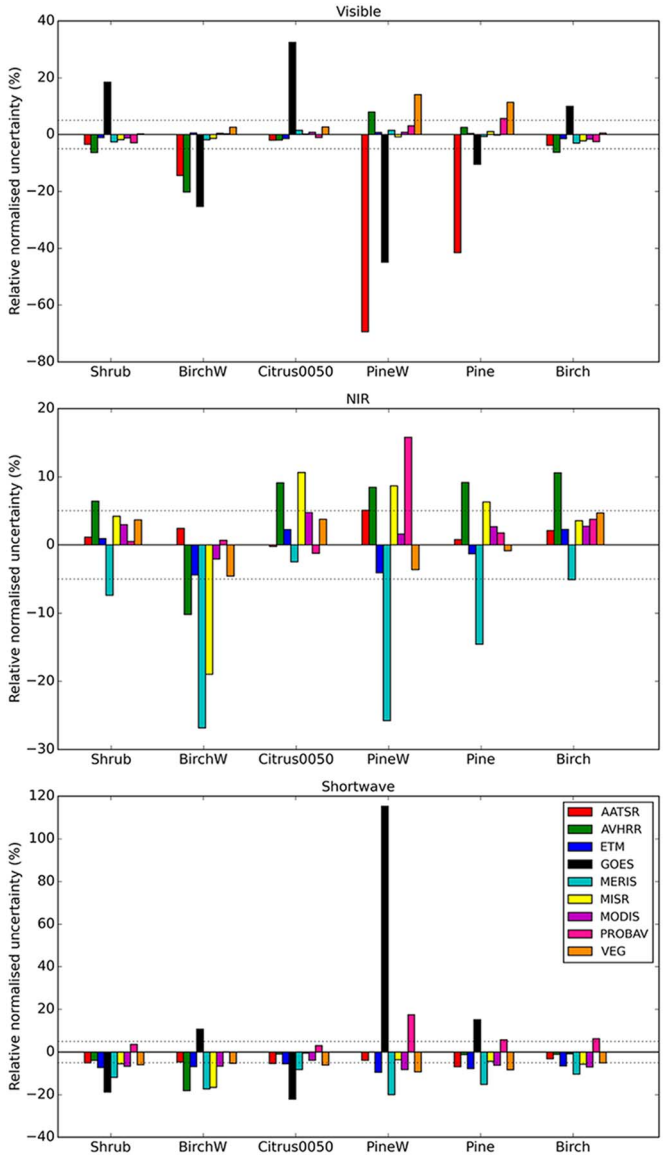

Fig. 2. Relative normalized uncertainty (Δ [%]) for $\mathrm{BBA_{vis}}$, $\mathrm{BBA_{nir}}$, and $\mathrm{BBA_{sw}}$ for canopies and all sensors, excluding MVIRI and SEVIRI, with (dotted line) GCOS 5% accuracy requirement. Shrub: Shrubland; BirchW: Birch stand winter; Citrus0050: Citrus SZA 50°, SAA 0°; PineW: Pine stand winter; Pine: Pine stand summer; Birch: Birch stand summer.

III. Results

Fig. 2 shows the relative normalized uncertainty (Δ [%]) of BBA computed from conversion formulas for each sensor for each canopy and each broad-band range for all sensors (excluding MVIRI and SEVIRI instruments). Results indicate that for $\mathrm{BBA_{vis}}$, AATSR, GOES-8 Imager, and, to some extent, AVHRR display larger uncertainties. AATSR, in particular, has larger (negative) Δ in an evergreen canopy (pine) in both summer and winter with uncertainties of -41.5% and -69.3% respectively. The GOES-8 Imager also displays larger uncertainties in the case of all canopy types, falling consistently outside the GCOS requirement (dotted line). The remaining sensors fall within or around the 5% GCOS requirement, where, on average, most sensors perform well in this broad-band range.

TABLE III
Overall Relative Normalized Uncertainty (Δ [%]) for $\mathrm{BBA_{vis}}$, $\mathrm{BBA_{nir}}$, and $\mathrm{BBA_{sw}}$ for All Canopies for Sensors (Except MVIRI/SEVIRI). Values Highlighted in Bold Represent Values Above the 5% GCOS Requirement

Sensor	Visible	NIR	Shortwave
AATSR	**-22.41287**	1.87635	-4.80237
AVHRR	-4.03479	**5.60949**	-4.17330
ETM+	-0.35828	-0.72435	**-7.21079**
GOES-8 Imager	-3.28959	-	**16.61754**
MERIS	-0.84131	**-13.6764**	**-13.76825**
MISR	-0.81229	2.41860	**-6.02509**
MODIS	-0.1385	2.10369	**-6.3968**
PROBA-V	0.42780	3.54628	**6.02038**
VEGETATION	**5.21281**	0.51115	**-6.62140**

For $\mathrm{BBA_{nir}}$, AVHRR, MERIS, and MISR exhibit larger uncertainties; in particular, MERIS displays consistent uncertainties, notably for an evergreen canopy (pine) in the winter and summer and a boreal canopy (birch) in the winter canopy which have values at -25.8%, -14.5%, and -26.8%, respectively. Although the uncertainties are not high, $\mathrm{BBA_{nir}}$ calculated from conversion formulas for both AVHRR and MISR often fall outside the GCOS requirement. The same sensors that comply with the GCOS requirement for $\mathrm{BBA_{vis}}$ also comply for $\mathrm{BBA_{nir}}$, namely, ETM+, MODIS, PROBA-V (with the exception of a pine-stand winter canopy), and VEGETATION. With respect to $\mathrm{BBA_{sw}}$, the GOES-8 Imager exhibits a large Δ (115.2%) for the pine-stand winter canopy and also for all other canopies with the exception of a birch-stand during the summer canopy. In addition, MERIS consistently displays larger negative uncertainties within this short-wave range for all canopies. Δ for this short-wave range appear, first, larger for all canopies and sensors than those in the visible and NIR and, second, consistently negative. Table III indicates the overall Δ for all canopies for each of the sensors, showing that, while MODIS, PROBA-V, and VEGETATION sensors are able to extract BBA with smaller uncertainties, AATSR, GOES-8 Imager, and MERIS appear less effective. Fig. 3 shows the results for MVIRI and SEVIRI sensors. For $\mathrm{BBA_{sw}}$, the broad-band range in which MVIRI sensors compute BBA, SEVIRI sensors show smaller uncertainties in comparison, whereas MVIRI sensors fall outside GCOS requirements for all canopies.

IV. Discussion

In terms of sensors, on average, ETM+, MISR, MODIS, PROBA-V, and VEGETATION conversion formulas are able to compute BBA with fairly low uncertainty and, in most canopies and broad-band ranges, are within the GCOS requirement. AATSR, GOES-8 Imager, and MERIS, on the other hand, display consistently larger Δ values, and their conversion formulas are less effective in extracting BBA. This is likely a direct result of the sensor wavebands used to compute BBA. The GOES-8 Imager uses only a single visible band to compute BBA values, and AATSR has four bands; however, the first band starts at only 555 nm and therefore misses part of the visible region, and that would explain the large Δ in this region. With respect to MERIS, the sensor wavebands only cover the region up to 1040 nm, which would again justify

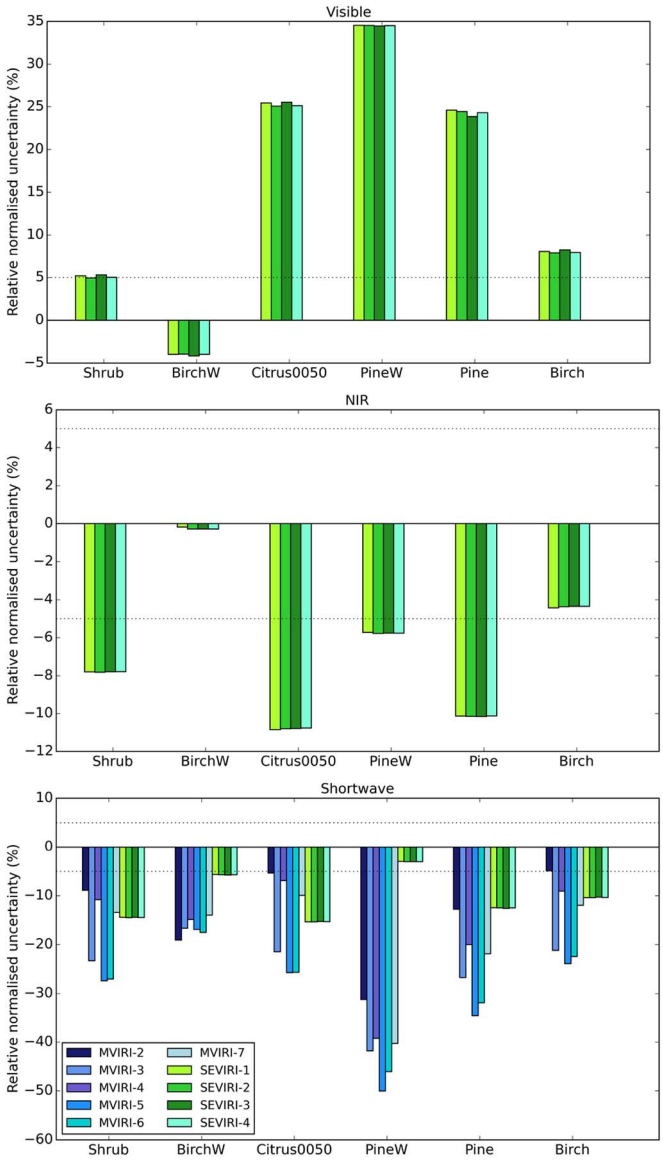

Fig. 3. Relative normalized uncertainty (Δ [%]) for $\mathrm{BBA_{vis}}$, $\mathrm{BBA_{nir}}$, and $\mathrm{BBA_{sw}}$ for canopies and MVIRI and SEVIRI sensors with (dotted line) GCOS 5% accuracy requirement. Shrub: Shrubland; BirchW: Birch stand winter; Citrus0050: citrus SZA 50°, SAA 0°; PineW: Pine stand winter; Pine: Pine stand summer; Birch: Birch stand summer.

the larger uncertainties, specifically in the NIR range and, to some extent, the short-wave range. The remaining sensors that show smaller Δ values likely perform better, either because they have many sensor wavebands, for example, ETM+ and MODIS, or the sensor wavebands cover most or all of the short-wave range, for example, PROBA-V and VEGETATION. MVIRI and SEVIRI appear to show a consistent negative Δ in the NIR and short-wave ranges, suggesting that BBA is consistently overestimated. SEVIRI was shown to compute BBA more accurately in comparison to MVIRI, particularly reducing uncertainties in the more complex canopies. This is again likely to be a result of the sensor wavebands used, as MVIRI sensors use only one large band on the narrow-band-to-broad-band conversion from 400 to 1100 nm, whereas SEVIRI uses three bands covering 560–1790 nm.

In terms of broad-band range, BBA can be extracted, on average, better in the visible and NIR. Specific sensors display exceptions to this, particularly AATSR and GOES-8 Imager in the visible and AVHRR, MERIS, and MISR in the NIR. The performance of conversion formulas within each broad-band range is a result of the wavelength range of the sensor wavebands, as mentioned previously. Uncertainties in the short-wave range are consistently negative, implying the underestimation of BBA. Similar results have been found in [16], which is likely due to a lack of sensor wavebands throughout the entire short-wave spectral range. Uncertainties in computing BBA are shown to be higher for more complex canopies, particularly for a boreal canopy (birch-stand) in the summer season and an evergreen canopy (pine-stand) during both winter and summer seasons. In particular, Δ values are highest for the evergreen winter canopy, as both snow and complex heterogeneous vegetation spectra contribute toward this complex spectral albedo signature. For simpler canopies such as shrubland and citrus orchard, BBA conversion formulas are more effective.

V. Conclusion

A 3-D MCRT model was used to simulate DHR for a variety of complex vegetation canopies; then, the accuracy of narrow-band-to-broad-band conversion formulas used to compute BBA was assessed. Accuracy depends on the sensor, ecosystem complexity, and the broad-band range of the BBA. ETM+, MODIS, PROBA-V, and VEGETATION sensors were shown to be able to convert to BBA with the lowest uncertainties, whereas AATSR, AVHRR, and MISR were shown to exhibit higher uncertainty in specific broad-band ranges and vegetation canopies, and the GOES-8 Imager and MERIS exhibited the highest uncertainties in most cases. Given that, on the ground, ecosystems are even more complex and varied than some of the canopies used in this letter, the target accuracy for BBA defined by GCOS is demanding when retrieved by space. The modeling approach used in this letter is beneficial as it allows complete control over the experiments; however, the high information requirement to describe a complex 3-D vegetation canopy means that not all ecosystem types can be covered. Subsequently, more albedo measurements using both modeling and field measurements in many ecosystem types would further improve the accuracy of narrow-band-to-broad-band conversion formulas.

References

[1] GCOS, "Systematic observation requirements for satellite-based data products for climate, update: Supplemental details to the satellite-based component of the implementation plan for the global observing system for climate in support of the UNFCC (2011 Update)," World Meteorol. Org., Geneva, Switzerland, Tech. Rep. GCOS-154, 2011.

[2] P. M. F. Forster and J. M. Gregory, "The climate sensitivity and its components diagnosed from earth radiation budget data," *J. Clim.*, vol. 19, no. 1, pp. 39–52, 2006.

[3] Y. Govaerts and A. Lattanzio, "Estimation of surface albedo increase during the eighties Sahel drought from Meteosat observations," *Global Planetary Change*, vol. 64, no. 3/4, pp. 139–145, 2008.

[4] E. A. Lyons, Y. Jin, and J. T. Randerson, "Changes in surface albedo after fire in boreal forest ecosystems of interior Alaska assessed using MODIS satellite observations," *J. Geo—Phys. Res., Biogeosci.*, vol. 113, 2008, Art. no. G02012.

[5] J. Schulz *et al.*, "Operational climate monitoring from space: The EUMETSAT Satellite Application Facility on Climate Monitoring (CM-SAF)," *Atmos. Chem. Phys.*, vol. 9, no. 5, pp. 1687–1709, 2009.
[6] B. Pinty *et al.*, "Surface albedo retrieval from Meteosat: 1. Theory," *J. Geophys. Res., Atmos.*, vol. 105, no. D14, pp. 18 099–18 112, 2000.
[7] Y. M. Govaerts, A. Lattanzio, M. Taberner, and B. Pinty, "Generating global surface albedo products from multiple geostationary satellites," *Remote Sens. Environ.*, vol. 112, no. 6, pp. 2804–2816, 2008.
[8] A. Loew and Y. Govaerts, "Towards multidecadal consistent meteosat surface albedo time series," *Remote Sens. Environ.*, vol. 2, no. 4, pp. 957–967, 2014.
[9] D. Aminou, "MSG's SEVIRI instrument," *ESA Bull.*, vol. 111, pp. 15–17, 2002.
[10] B. Geiger and O. Samain, "Albedo determination, algorithm theoretical basis document of the cyclopes project, version 2.0," Tech. Rep., Météo-France/CNRM, Paris, France, 2004.
[11] C. B. Schaaf *et al.*, "First operational BRDF, albedo nadir reflectance products from MODIS," *Remote Sens. Environ.*, vol. 83, no. 12, pp. 135–148, 2002.
[12] D. Diner *et al.*, "Multiangle Imaging Sprectroradiometer (MISR) Level 2 Top-of-Atmosphere Albedo Algorithm Theoretical Basis," Revision D, Jet Propulsion Lab., California Inst. Technol., Pasadena, CA, USA, Tech. Rep. PL Rep. D-13401, Dec. 1999.
[13] J.-P. Muller *et al.*, "Globalbedo Algorithm Theoretical Basis Document," Tech. Rep., GlobAlbedo Consortium, Surrey, U.K., 2013.
[14] N. Liu, Q. Liu, L. Wang, and J. Wen, "A temporal filtering algorithm to reconstruct daily albedo series based on glass albedo product," in *Proc. IEEE IGARSS*, Jul. 2011, pp. 4277–4280.
[15] J. V. Martonchik, C. J. Bruegge, and A. H. Strahler, "A review of reflectance nomenclature used in remote sensing," *Remote Sens. Rev.*, vol. 19, no. 1–4, pp. 9–20, 2000.
[16] J. I. Peltoniemi *et al.*, "Land surface albedos computed from BRF measurements with a study of conversion formulae," *Remote Sens.*, vol. 2, no. 8, p. 1918, 2010.
[17] S. Liang *et al.*, "Narrowband to broadband conversions of land surface albedo: II. Validation," *Remote Sens. Environ.*, vol. 84, no. 1, pp. 25–41, 2003.
[18] M. Disney, P. Lewis, G. Thackrah, T. Quaife, and M. Barnsley, "Comparison of MODIS broadband albedo over an agricultural site with ground measurements and values derived from earth observation data at a range of spatial scales," *Int. J. Remote Sens.*, vol. 25, no. 23, pp. 5297–5317, 2004.
[19] Y. M. Govaerts and M. M. Verstraete, "Raytran: A Monte Carlo ray-tracing model to compute light scattering in three-dimensional heterogeneous media," *IEEE Trans. Geosci. Remote Sens.*, vol. 36, no. 2, pp. 493–505, Mar. 1998.
[20] J.-L. Widlowski *et al.*, "The fourth phase of the radiative transfer model intercomparison (RAMI) exercise: Actual canopy scenarios and conformity testing," *Remote Sens. Environ.*, vol. 169, pp. 418–437, 2015.
[21] B. Pinty *et al.*, "Radiation transfer model intercomparison (RAMI) exercise," *J. Geophys. Res.*, vol. 106, pp. 11 937–11 956, 2001.
[22] A. Kuusk, T. Nilson, M. Paas, M. Lang, and J. Kuusk, "Validation of the forest radiative transfer model FRT," *Remote Sens. Environ.*, vol. 112, no. 1, pp. 51–58, 2008.
[23] A. Kuusk, J. Kuusk, and M. Lang, "A dataset for the validation of reflectance models," *Remote Sens. Environ.*, vol. 113, no. 5, pp. 889–892, 2009.
[24] A. Kuusk, T. Nilson, J. Kuusk, and M. Lang, "Reflectance spectra of RAMI forest stands in Estonia: Simulations and measurements," *Remote Sens. Environ.*, vol. 114, no. 12, pp. 2962–2969, 2010.
[25] B. Kötz *et al.*, "Radiative transfer modeling within a heterogeneous canopy for estimation of forest fire fuel properties," *Remote Sens. Environ.*, vol. 92, no. 3, pp. 332–344, 2004.
[26] F. Morsdorf *et al.*, "Lidar-based geometric reconstruction of boreal type forest stands at single tree level for forest and wildland fire management," *Remote Sens. Environ.*, vol. 92, no. 3, pp. 353–362, 2004.
[27] F. Morsdorf, B. Kötz, E. Meier, K. I. Itten, and B. Allgwer, "Estimation of LAI and fractional cover from small footprint airborne laser scanning data based on gap fraction," *Remote Sens. Environ.*, vol. 104, no. 1, pp. 50–61, 2006.
[28] J. Stuckens, B. Somers, S. Delalieux, W. W. Verstraeten, and P. Coppin, "The impact of common assumptions on canopy radiative transfer simulations: A case study in citrus orchards," *J. Quant. Spectr. Radiative Transfer*, vol. 110, no. 12, pp. 1–21, 2009.
[29] M. Jung, M. Reichstein, and A. Bondeau, "Towards global empirical upscaling of FLUXNET eddy covariance observations: Validation of a model tree ensemble approach using a biosphere model," *Biogeosciences*, vol. 6, no. 10, pp. 2001–2013, 2009.
[30] R. Lacaze, "Gio Global Land Component Lot 1 (GIO-GL Lot 1): Algorithm Theoretical Basis Document Surface Albedo," Copernicus Brussels, Belgium, Tech. Rep., 2014.
[31] S. Liang, "Narrowband to broadband conversions of land surface albedo I: Algorithms," *Remote Sens. Environ.*, vol. 76, no. 2, pp. 213–238, 2001.
[32] "Algorithm theoretical basic document: Land surface Albedo," LSA SAF, Plano, TX, USA, Tech. Rep., 2012.